Available online at www.sciencedirect.com
ScienceDirect
Trans. Nonferrous Met. Soc. China 30(2020) 1884−1894
Transactions of Nonferrous Metals Society of China
www.tnmsc.cn

Decomposition kinetics of carbon-doped FeCoCrNiMn high-entropy alloy at intermediate temperature

Jian PENG[1], Zi-yong LI[1], Xin-bo JI[1], Yan-le SUN[1], Li-ming FU[1,2,3], Ai-dang SHAN[1,2,3]

1. School of Materials Science and Engineering, Shanghai Jiao Tong University, Shanghai 200240, China;
2. Collaborative Innovation Center for Advanced Ship and Deep-sea Exploration (CISSE), Shanghai Jiao Tong University, Shanghai 200240, China;
3. Shanghai Key Laboratory of High Temperature Materials and Precision Forming, Shanghai Jiao Tong University, Shanghai 200240, China

Received 17 December 2019; accepted 3 June 2020

Abstract: Phase decomposition kinetics and the corresponding mechanical properties of the severe cold-rolled (SCRed) carbon-doped (1.3 at.%) equimolar FeCoCrNiMn high-entropy alloy (HEA) after being annealed at 500 °C were investigated. This single face-centered cubic (FCC) solid-solution HEA decomposed to $M_{23}C_6$+$L1_0$, *B*2, and σ in chronological order. The formation kinetics of the $L1_0$, *B*2, and σ phases followed the Johnson−Mehl−Avrami−Kolmogorov (JMAK) equation. The yield strength of the HEA was 1520 MPa and increased to 1920 MPa after being annealed at 500 °C for 1 h, as a result of the formation of nanosized $M_{23}C_6$ and $L1_0$. Both strength and ductility decreased after 2 d of annealing due to the increase of volume fractions and the coarsening of the $M_{23}C_6$ and $L1_0$ precipitates. From 4 to 32 d, the hardness was found to increase, which is ascribed to the rapid formation of the *B*2 and σ phases. From 32 to 64 d, the hardness increased further to finally reach about HV 760, with the FCC matrix almost exhausted to form the $M_{23}C_6$, $L1_0$, *B*2, and σ phases. The results of this work may serve as a guide for the heat-treatment of carbon-doped HEAs.

Key words: FeCoCrNiMn; high-entropy alloy; decomposition kinetics; mechanical properties; carbon doping

1 Introduction

High-entropy alloys (HEAs) are a class of multi-principal element materials that form solid solutions with high configurational entropy [1]. Equiatomic FeCoCrNiMn is a well-established single face-centered cubic (FCC) solid-solution HEA [2−5]. It has garnered scientific interest because of its properties such as excellent toughness at cryogenic temperatures, high strain hardening [2], and good resistance to hydrogen embrittlement [3].

However, the yield strength of the cast FeCoCrNiMn alloy is only 209 MPa [6]. The strengthening of grain boundaries and the addition of carbon have been widely utilized to increase the yield strength [7−12]. Detailed studies have also been conducted on the effects of carbon addition on the microstructure and the mechanical properties of FeCoCrNiMn alloy [10−12]. A yield strength of ~1030 MPa, with a uniform elongation of ~11%, was achieved by combining the effect of $M_{23}C_6$ carbide precipitation and grain boundary strengthening in carbon-doped HEAs [10].

Recent scientific literatures have shown that most HEAs tend to decompose after prolonging annealing time at intermediate temperatures [13−16].

Foundation item: Project (51901134) supported by the National Natural Science Foundation of China; Project (SJTU.18X100040023) supported by the Program of Scientific Research Ability Cultivation for Young Researchers, China
Corresponding author: Li-ming FU, Tel: +86-21-54748974, Fax: +86-21-54740825, E-mail: lmfu@sjtu.edu.cn;
Ai-dang SHAN, Tel: +86-21-54747556, Fax: +86-21-54740825, E-mail: adshan@sjtu.edu.cn
DOI: 10.1016/S1003-6326(20)65347-X

A Cr-rich σ phase forms in FeCoCrNiMn HEA, after being annealed at 600−700 °C [14,17], while three different phases ($L1_0$, BCC, and $B2$) are observed after being annealed at 500 °C [14]. Based on the decomposition kinetics, it is feasible to design high yield strength HEAs with ample elongation utilizing the decomposition process in a Cr-rich FeCoCrNiMn HEA [18,19]. The decomposition behavior of HEAs is sensitive to chemical composition [15,19,20]. For example, increasing the Cr concentration enhances the high-temperature stability of the σ phase in FeCoCrNiMn-type HEAs [19], while increasing the Ni content inhibits the formation of the σ phase [20].

In our recent work [9], we have investigated the precipitation strengthening of carbides in a severely cold-rolled (SCRed) 1.3 at.% carbon-doped equimolar FeCoCrNiMn HEA, which was close to the ultimate solid solubility of carbon [21]. In this work, we focused on decomposition during the annealing process at intermediate temperatures. The underlying decomposition kinetics and evolution of the mechanical properties of carbon-doped FeCoCrNiMn were investigated based on a comparison of the microstructure and mechanical properties.

2 Experimental

The HEA was prepared in a tungsten electrode arc furnace using commercial pure metals, Fe, Co, Cr, Ni, and Mn (>99.95 wt.%), and Fe−4.2wt.%C alloy. The cast ingot, with dimensions of 80 mm × 30 mm × 10 mm, was homogenized at 1220 °C for 6 h, then SCRed to a thickness of 0.5 mm, with a 95% reduction. Inductively coupled plasma optical emission spectrometer (iCAP7600) and a frequency infrared ray carbon combustion analyzer (G4 ICARUS) were used to characterize the chemical composition (Table 1). The SCRed single FCC-structured HEA was then isothermally annealed at 500 °C for 1, 3, 6, or 12 h, and 1, 2, 4, 8, 16, 32, or 64 d.

A Shimadzu XRD−6000 X-ray diffraction (XRD) instrument with Cu K_α radiation (λ= 0.154 nm) operating at 35 kV and a tube current of 200 mA, was used to analyze the phase constitution at a scanning rate of 2 (°)/min. The as-cast and homogenized specimens were etched using a solution of 5 g of $CuCl_2$ in a mixture of 100 mL of HCl and 100 mL of C_2H_5OH, after which the microstructure of the HEAs was examined using a ZEISS optical microscope (OM). A vibration polishing machine was used to polish the electron backscattering diffraction (EBSD) samples. To reduce inconsistencies in sample preparation, all samples were embedded into a mounting for grinding and polishing. The microstructures of the annealed HEAs were examined using a TENSCAN MIRA3 scanning electron microscope (SEM) equipped with energy-dispersive X-ray spectroscopy (EDS) and EBSD detectors. The scanning step for the EBSD measurement was 30 nm, and $B2$ (FeCo, $Pm\bar{3}m$, ICSD No. 56273), $L1_0$ (NiMn, $P4/mmm$, ICSD No. 104916), and σ ($P42/mnm$, ICSD No. 102747) phases were used to index the EBSD results. Wild spikes and decomposition phases with grain sizes below 50 nm underwent a clean-up procedure. A JEM−2100F transmission electron microscope (TEM) was employed to characterize the decomposition. The foils for TEM observation were obtained by twin-jet electrochemical polishing in an electrolyte consisting of 5% perchloric acid and 95% ethanol at −30 °C. The average size of the decomposition phases was defined using the area-equivalent diameter.

Table 1 Chemical composition of homogenized FeCoCrNiMn−1.3C HEA

Element	Molar fraction/%	Mass fraction/%
Fe	19.42	19.55
Co	20.06	21.28
Cr	20.14	21.36
Ni	19.75	19.53
Mn	19.27	18.01
C	1.36	0.29

Hardness measurements were conducted on a Zwick Roell hardness tester with a Vickers diamond pyramid indenter using a load of 500 g and a dwell time of 15 s. The average value of at least seven points was taken as the effective value of each sample. Uniaxial tensile testing was performed on a Zwick universal testing machine using dog-bone tensile samples with a gauge length of 10 mm and a gauge width of 3 mm at a strain rate of 5×10^{-4} s^{-1}. The elongation of each sample was measured using

the extensometer of the Zwick universal testing machine.

3 Results and discussion

3.1 Microstructure of HEA before decomposition

Figure 1 shows OM images and the corresponding XRD patterns of the as-cast and homogenized specimens. Noticeable particles, confirmed to be $M_{23}C_6$ particles according to the XRD patterns and recent reports, exist at the grain boundaries of the cast specimen [9,10]. After homogenization annealing at 1220 °C, a single-phase FCC HEA with coarse grains was obtained [9]. It exhibits an FCC structure with homogeneous composition after being SCRed, as illustrated in the EBSD phase distribution (PD) and EDX maps (Fig. 2).

3.2 Decomposition sequence during annealing at 500 °C

To determine the decomposition sequence, the phase constitution and distribution of the HEA after being annealed for various durations were measured by XRD (Fig. 3). The XRD pattern of the specimen after being annealed for 1 h showed a single solid-solution FCC structure, while *B*2, $L1_0$, and $M_{23}C_6$ diffraction peaks were observed after being annealed for 2 d. The σ phase appeared when the annealing time was increased to 4 d, and the peak intensities of the decomposed phases were increased after being annealed for 4−16 d. Finally, the FCC structured HEA was completely decomposed to *B*2, $L1_0$, $M_{23}C_6$, and σ phases after being annealed for 64 d.

EBSD results further illustrate the microstructure evolution of the HEA during the annealing process (Fig. 4). The $M_{23}C_6$ phase was not considered during the EBSD measurement as indexing the $M_{23}C_6$ phase would result in mis-indexing of the FCC phase. The PD map of the HEA annealed for 1 h showed the FCC single solid−solution structure. Noticeable $L1_0$ grains started to appear in the FCC matrix after 12 h of annealing, while *B*2 grains were only detected after being further annealed for 2 d. After being annealed

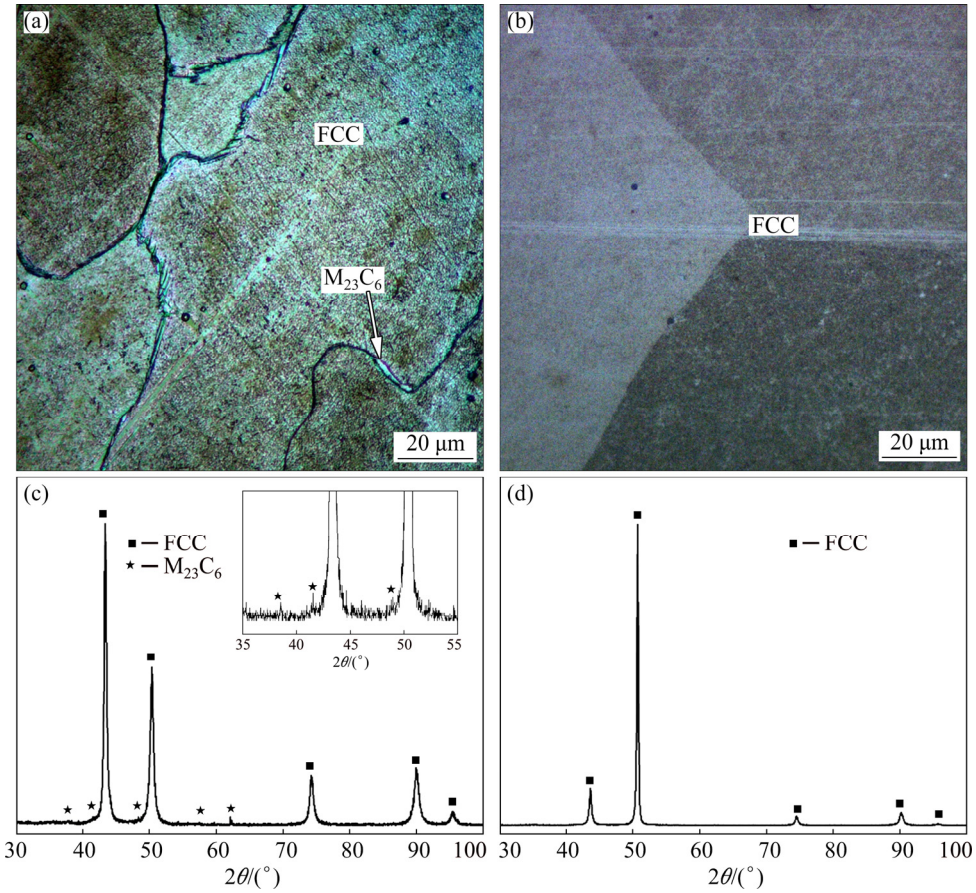

Fig. 1 OM images (a, b) and corresponding XRD patterns (c, d) of FeCoCrNiMn−1.3C HEA: (a, c) As-cast; (b, d) Homogenized

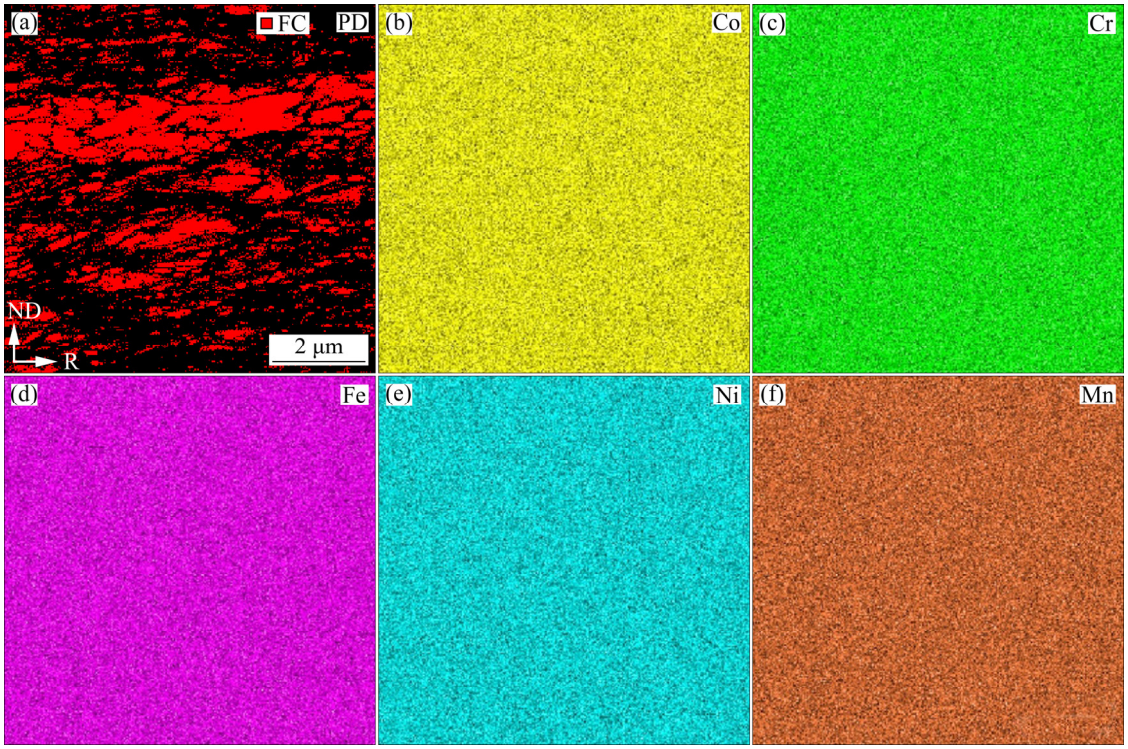

Fig. 2 Microstructures of SCRed HEA: (a) PD map; (b−f) EDX maps

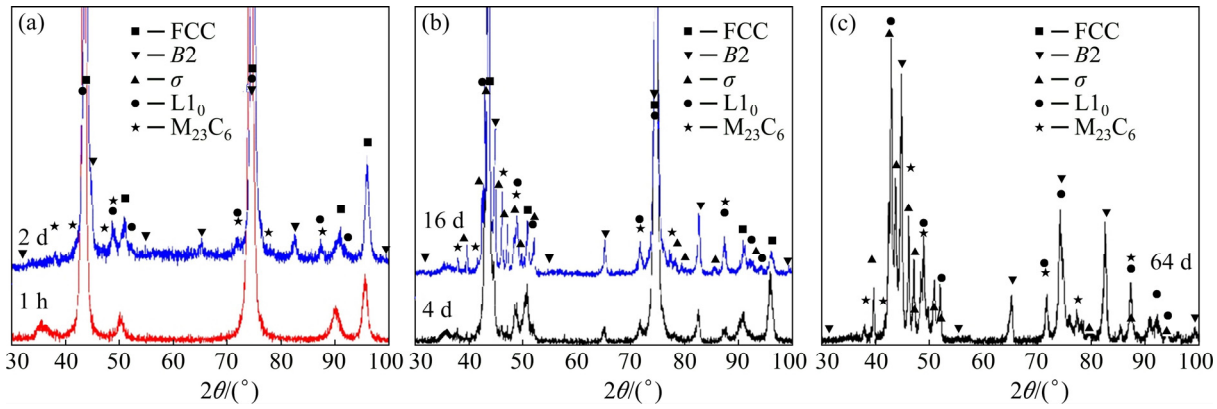

Fig. 3 XRD patterns of FeCoCrNiMn−1.3C HEA after being annealed for various durations: (a) 1 and 2 d; (b) 4 and 16 d; (c) 64 d

for 4 d, σ grains were observed. The area fractions of $B2$, $L1_0$, and σ phases increased as annealing further proceeded, and the FCC phase was almost completely decomposed after being annealed for 32 d. Further extending the annealing time to 64 d resulted in complete decomposition of the FCC phase.

It should be noted that $M_{23}C_6$ and $L1_0$ grains already existed in the HEA after being annealed for 1 h. The grains were not found in the PD map as the detection limits of EBSD and XRD analyses were not attained. The TEM observation proved the existence of $M_{23}C_6$ precipitate, as illustrated in Figs. 5(a–c). Moreover, long-range ordered structures of about 5 nm in size were randomly distributed in the HEA matrix, as shown in the high-resolution TEM (HRTEM) image in Fig. 5(d). According to the fast Fourier transform (FFT) patterns (Figs. 5(e–g)) of the selected regions, these structures were either $L1_0$ or $M_{23}C_6$ nano-grains. This finding is consistent with a previous report on equimolar FeCoCrNiMn HEA, in which a long-range ordered structure was also formed [22].

When the annealing time was increased to 2 d, the $L1_0$ and $M_{23}C_6$ grains became coarser while the

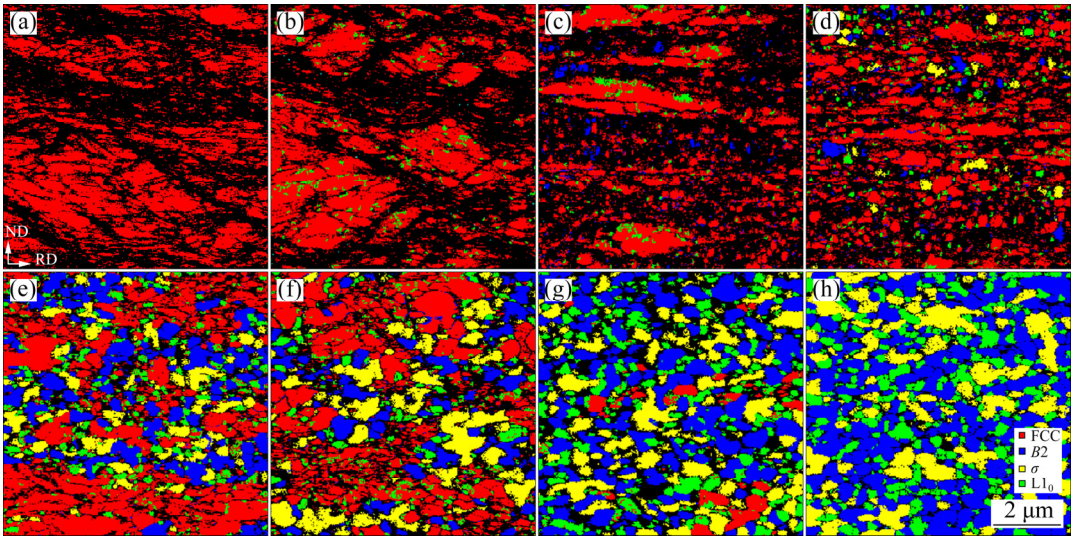

Fig. 4 EBSD PD maps of HEA after being annealed at 500 °C for various durations: (a) 1 h; (b) 12 h; (c) 2 d; (d) 4 d; (e) 8 d; (f) 16 d; (g) 32 d; (h) 64 d

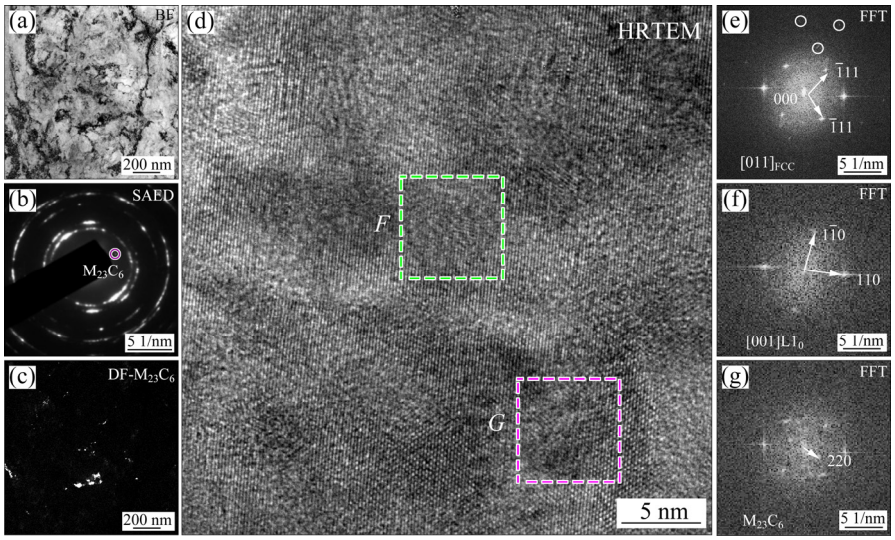

Fig. 5 TEM images of HEA after being annealed for 1 h: (a) Bright field (BF) image; (b) SAED pattern of (a); (c) Dark field (DF) image of selected diffraction spot of $M_{23}C_6$ in (b); (d) HRTEM image; (e) FFT pattern of entire region of (d); (f) FFT pattern of Region *F* in (d); (g) FFT pattern of Region *G* in (d)

*B*2 grains appeared (Fig. 6). Extra spots of *B*2, $L1_0$, and $M_{23}C_6$ grains were found in the SAED pattern besides the diffraction rings of the FCC phase. DF images of the representative diffraction spots showed the morphology and distribution of the FCC, $M_{23}C_6$, $L1_0$, and *B*2 grains.

The HEA was almost completely decomposed after being annealed at 500 °C for 64 d, as shown in Fig. 4(h). Almost no FCC phase could be detected, while four phases, that is, *B*2, $L1_0$, σ, and $M_{23}C_6$, were observed in the XRD pattern of the HEA annealed for 64 d. The FD and EDX maps further illustrate the phase morphology of the *B*2, $L1_0$, and σ phases, and the corresponding element concentrations in the HEA annealed for 64 d (Fig. 7). Apparently, the *B*2 phase is rich in Fe and Co, the $L1_0$ phase is rich in Ni and Mn, and the σ phase is rich in Cr. The average grain sizes of the *B*2, $L1_0$, and σ phases were found to be (0.53±0.20), (0.24±0.08), and (0.63±0.22) μm, respectively.

It should be noted that the *B*2 ordered phase, rather than the disordered BCC or BCC+*B*2 phases, was formed in the present HEA, which was confirmed by the XRD pattern of the annealed HEA (Fig. 3), the EBSD element concentration maps (Fig. 7), and the SAED patterns (Figs. 8(d−f)) of a

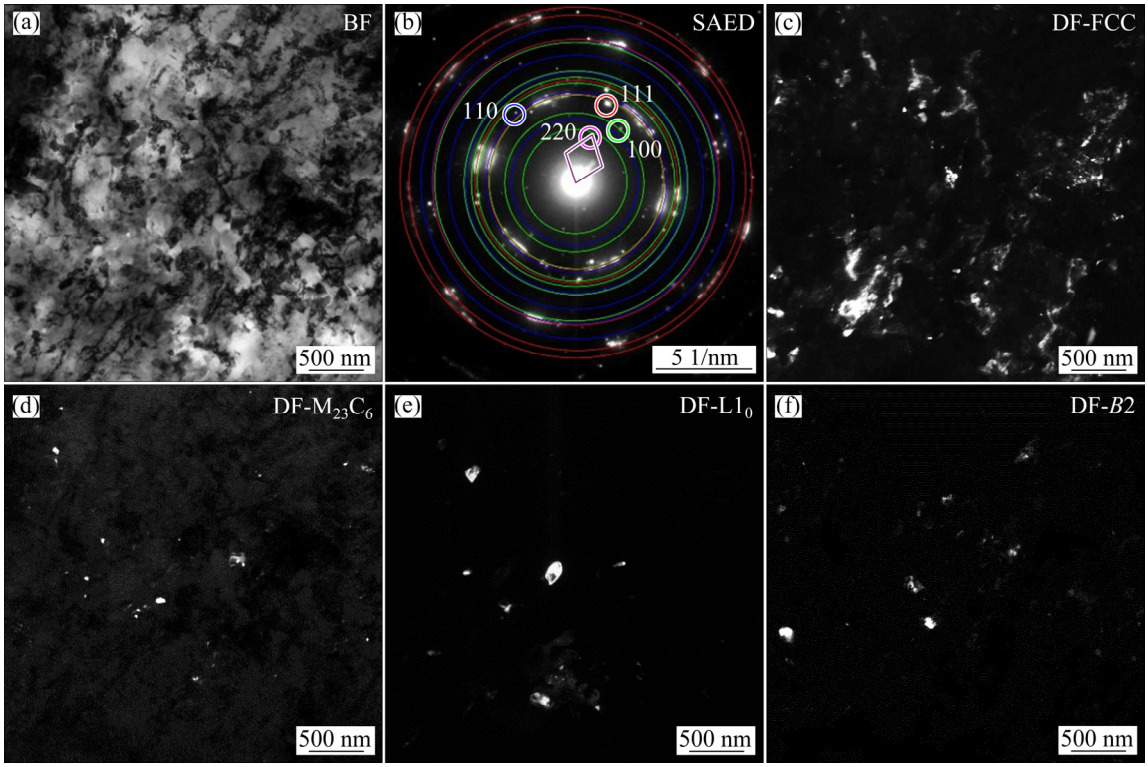

Fig. 6 TEM images of HEA after being annealed for 2 d: (a) BF image; (b) SAED pattern of (a); (c−f) DF images of selected diffraction spots illustrating morphology and distribution of FCC (c), $M_{23}C_6$ (d), $L1_0$ (e), and *B*2 (f) phases

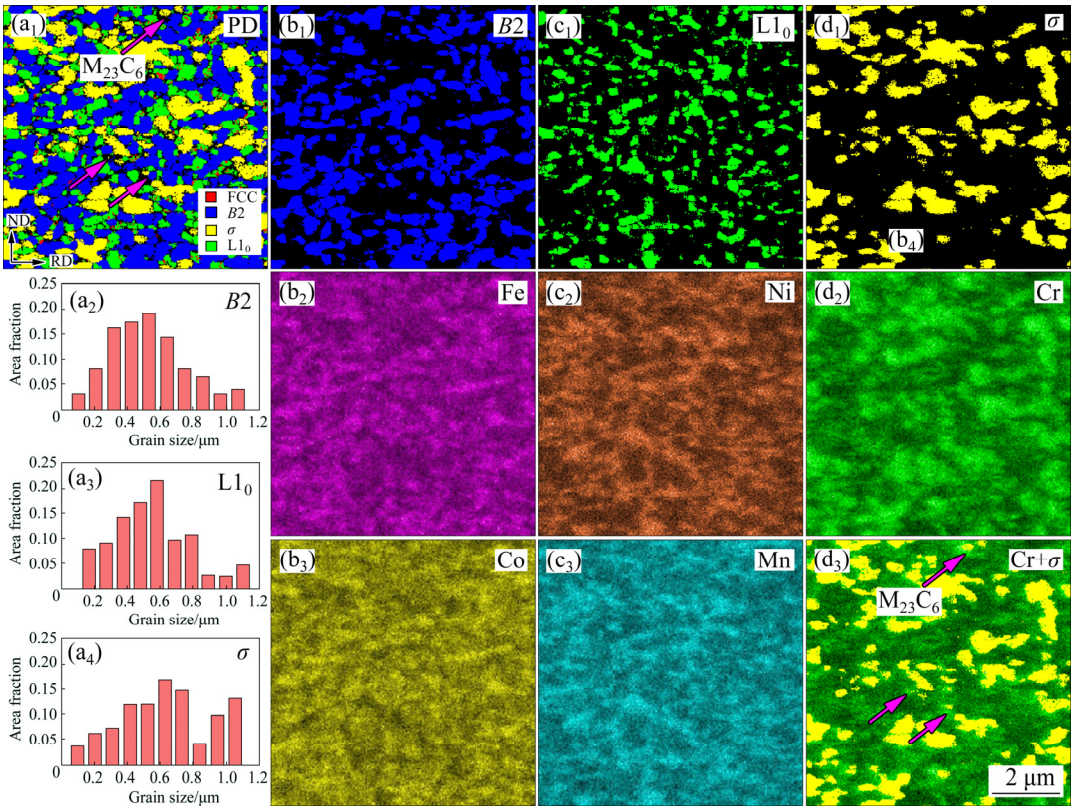

Fig. 7 Microstructures of HEA after being annealed for 64 d: (a_1−a_4) PD map and grain size distribution histograms of each phase; (b_1−b_3) PD map of *B*2 and EDX concentration maps of Fe and Co; (c_1−c_3) PD map of $L1_0$ and EDX concentration maps of Ni and Mn; (d_1−d_3) PD map of σ and EDX concentration map of Cr (Unsolved regions in PD map (a_1) and its Cr-rich characteristic (d_3) corresponding to existing $M_{23}C_6$ grains)

representative *B*2 grain (Fig. 8(a)). In addition, the grain distribution was consistent with the elemental concentrations of Co and Fe (Figs. 7(b_2) and (b_3)). As reported by OTTO et al [14], the *B*2 phase in the equimolar FeCoCrNiMn HEA was rich in Fe and Co, while the disordered BCC was rich in Cr [14]. Thus, it should be the *B*2 phase that was formed after being annealed for 64 d.

In addition to the $L1_0$, *B*2, and σ phases, the $M_{23}C_6$ carbide, i.e., the most common precipitate, in the carbon-doped FeCoCrNiMn-type HEAs [7,8,10,23−26], was also formed in the HEA after being annealed for 64 d. Some unsolved regions in the PD map (Fig. 7(a_1)), which are characterized as Cr-rich (Fig. 7(d_3)), correspond to the bulky $M_{23}C_6$ grains that are equally rich in Cr [10]. The morphology and distribution of the $M_{23}C_6$ phase are further illustrated in the TEM BF image, corresponding to the SAED pattern and the DF image (Figs. 8(a, b, c)).

The addition of carbon in FeCoCrNiMn HEA altered the decomposition sequence. In the present carbon-doped HEA, the $M_{23}C_6$+$L1_0$, *B*2, and σ phases occurred sequentially after prolonging annealing time at 500 °C. In contrast, only the *B*2, $L1_0$, and BCC phases were found in the equimolar FeCoCrNiMn HEA after being annealed at 450−500 °C [13,14].

The compositional grain boundary (GB) segregation is considered as a precursory state for phase nucleation in the FeCoCrNiMn HEA [16]. The co-segregation of Ni and Mn, with the corresponding co-depletion of Cr, Fe, and Co, occurred in the GBs. A slight enrichment of Cr was also observed in the GB regions, which were devoid of Ni or Mn segregation, indicating that a new phase nucleation occurred at the GBs. Hence, the Ni- and Mn-rich $L1_0$, and Cr-rich BCC were initially formed followed by the formation of a Fe- and Co-rich phase (*B*2) in the carbon-free FeCoCrNiMn HEA [14,16].

In the carbon-doped FeCoCrNiMn HEA, co-segregation of Ni and Mn might have induced the formation of $L1_0$ at GBs as C also tended to rapidly segregate at GBs [16], and $M_{23}C_6$ grains were prone to form in the Cr-rich GB regions devoid of Ni and Mn segregation. Then, *B*2 phase formed was characterized by Fe and Co depletion. Finally, a Cr-rich σ phase appeared with the co-depletion of Fe, Co, Ni, Mn, and C. Hence, the carbon-doped HEA followed the decomposition sequence of $M_{23}C_6$+$L1_0$, *B*2, and σ.

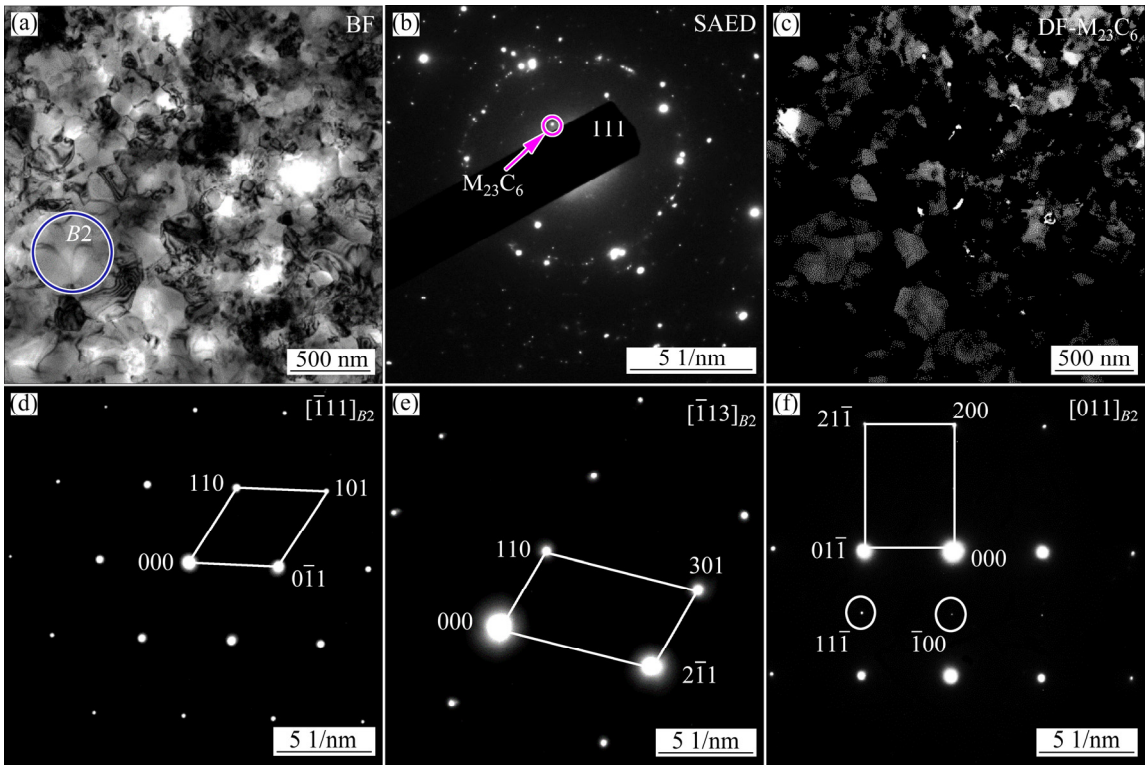

Fig. 8 TEM images of HEA annealed for 64 d: (a) BF image; (b) SAED pattern of selected region in (a); (c) DF image of selected diffraction spot of $M_{23}C_6$ phase in (b); (d−f) Corresponding SAED patterns of selected grain in (a)

3.3 Effect of phase decomposition on mechanical properties

The mechanical properties (Fig. 9) and decomposition kinetics (Fig. 10) of the HEA during the annealing process further illustrate the effect of adding carbon to the FeCoCrNiMn HEA. The hardness of the SCRed HEA was HV 500, which rapidly increased to HV 575 after being annealed for 1 h. Sequentially, it decreased slightly from HV 575 to HV 522 when the annealing time was increased from 1 h to 2 d. An abrupt increase in hardness was observed as the annealing process continued for 4−32 d. Finally, the hardness was steadied at about HV 760 after being annealed for 32−64 d. Compared with carbon-free FeCoCrNiMn HEA [13,22,27], the carbon-doped HEA showed a decrease in hardness after medium-term decomposition.

The stress–strain curves of representative specimens subjected to different annealing treatments are compared in Fig. 9(b). Table 2 lists the yield strength (YS) and uniform elongation (δ) of these specimens. The yield strength of the SCRed HEA was 1520 MPa and increased to 1920 MPa after being annealed for 1 h. Further annealing for 2 d led to a decrease in strength and a

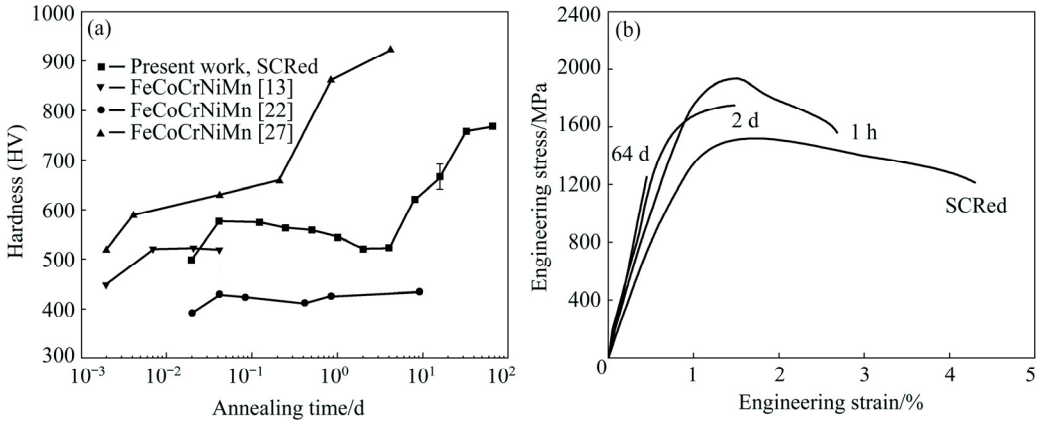

Fig. 9 Mechanical properties of annealed HEA: (a) Hardness−annealing time curves of carbon-doped FeCoCrNiMn HEA compared with carbon-free FeCoCrNiMn HEA [13,22,27]; (b) Engineering stress−engineering strain curves of representative samples

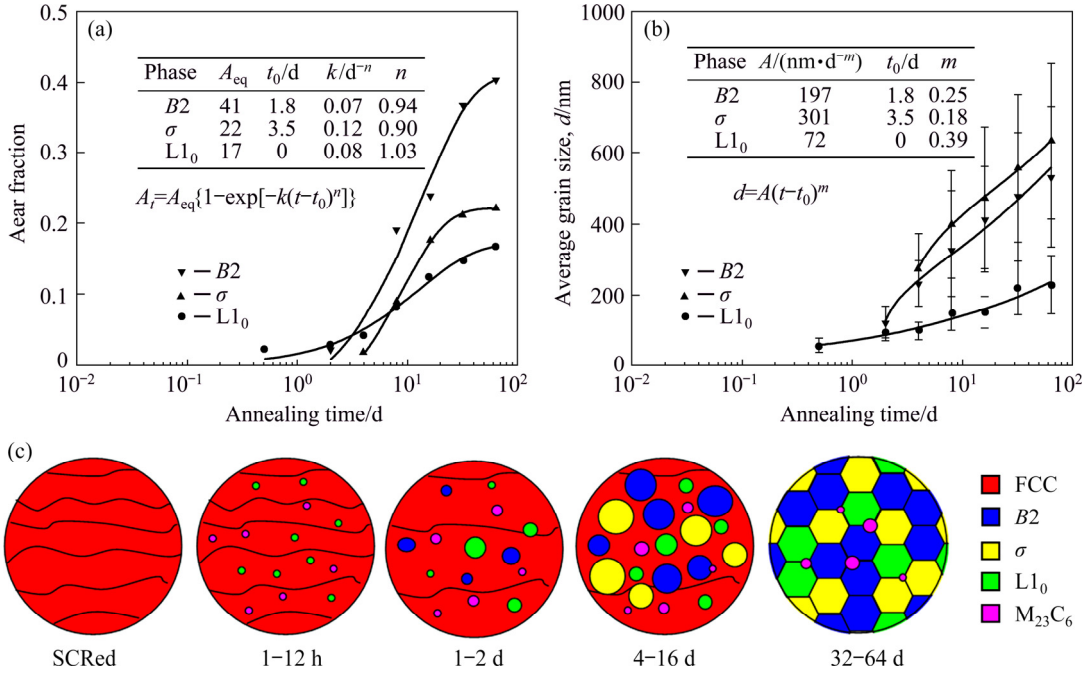

Fig. 10 Decomposition kinetics of HEA after being annealed at 500 °C: (a) Area fraction−annealing time curves of $B2$, $L1_0$, and σ phases; (b) Average grain size−annealing time curves of $B2$, $L1_0$, and σ phases; (c) Schematic diagrams of decomposition sequence

Table 2 Yield strength and uniform elongation of representative specimens

Condition	YS/MPa	δ/%
SCRed	1520	3.1
Annealed for 1 h	1920	1.5
Annealed for 2 d	1576	0.5
Annealed for 64 d	1252	0

simultaneous loss of ductility. For the 64 d annealing treatment, failure occurred in the elastic regime of the tensile test.

The formation of nanosized $M_{23}C_6$ and $L1_0$ grains resulted in the strengthening of the SCRed HEA after being annealed for 1 h. The carbon-doped HEA presented a yield strength of 1920 MPa and 1.5% uniform elongation after being annealed for 1 h. In this study, the increase in the hardness of FeCoCrNiMn HEA after being annealed at 500 °C for 1 h was consistent with that reported previously following similar being annealed conditions, which was from HV 394 to HV 430 because of the formation of a long-range ordered structure [13,22,27]. However, the FeCoCrNiMn HEA that underwent annealing for 1 h showed a sudden failure before yielding, with an ultimate tensile strength of only 1300 MPa [22]. Apparently, the nanosized $M_{23}C_6$ and $L1_0$ grains are responsible for the balanced strength and elongation after being annealed in this carbon-doped HEA.

The hardness and yield strength of the HEA slightly decreased when the annealing time increased from 1 h to 2 d. By employing the Williamson−Hall method [28,29] for analysis of the XRD patterns (Fig. 3(a)), the lattice constant (a) and micro-strain (ε) of the FCC matrix were calculated to be 0.3601 nm and 0.462%, respectively, for the sample annealed for 1 h, and 3.5911 nm and 0.384%, respectively, for the sample annealed for 2 d. The decrease in the lattice parameter of the FCC matrix was primarily a result of the occurrence of precipitation during the annealing process; consequently, the solid−solution strengthening effect decreased [30,31]. The dislocation density (ρ) can be derived from $\rho=2\sqrt{3}\varepsilon/(db)$ (b=0.254 nm) [29], where the average grain size (d) can be obtained from the EBSD measurement (250 nm after 1 h of annealing and 548 nm after 2 d of annealing). The dislocation density was estimated to be approximately 2.54×10^{14} m^{-2} and 0.96×10^{14} m^{-2} after being annealed for 1 h and 2 d, respectively. Moreover, the average grain sizes of the $M_{23}C_6$ and $L1_0$ phases increased after being annealed for 2 d (Fig. 4(c)). This grain coarsening resulted in a decrease in the elongation of the HEA after being annealed for 2 d (Fig. 9(b)). To summarize, concurrent precipitation from the solid−solution matrix and coarsening of the decomposition phases accompanied with the decrease in dislocation density, resulted in reduced hardness, yield strength, and elongation of the HEA after being annealed for 2 d.

When the annealing process was prolonged (4−32 d), an abrupt increase in hardness was observed, resulting from the rapid decomposition of the FCC matrix and the coinstantaneous formation of the $B2$ and σ phases (hard phases in HEAs) [18,32]. The Johnson−Mehl−Avrami−Kolmogorov (JMAK) equation (Eq. (1)) can be used to describe the decomposition kinetics of the $B2$, $L1_0$, and σ phases [33]:

$$A_t = A_{\text{eq}}\{1-\exp[-k(t-t_0)^n]\} \quad (1)$$

The average grain diameters (d) of the $B2$, $L1_0$, and σ phases were fitted in the following equation:

$$d=A(t-t_0)^m \quad (2)$$

where A_t ($0<A_t<A_{\text{eq}}$) is the surface area fraction for each phase of the HEA that underwent annealing for various durations t, A_{eq} is the final surface area fraction after reaching thermodynamic equilibrium, k is a rate constant, n is an exponent, t_0 represents the threshold time of precipitate formation, A is the growth rate constant, and m is the grain growth exponent. The rapid growth stage of the $B2$ and σ phases (Fig. 10) was consistent with the abrupt increase in hardness after being annealed for 4−32 d (Fig. 9(a)).

The fractions of the $B2$, $L1_0$, and σ phases approached thermodynamic equilibrium after being annealed for 32−64 d, as illustrated in Fig. 10(a). The 95% reduction in thickness that induced a high density of grain boundaries, was responsible for the rapid decomposition [13,16]. Grain boundaries and defects offered fast diffusion pathways and provided a pathway for concentration segregation and phase nucleation [16]. Consequently, the deformed HEAs with fine-grained microstructures decomposed faster than the coarse-grained HEAs. In the present work, SCRed HEA was almost

completely decomposed after being annealed for 32−64 d. The failure occurred in the elastic regime of the tensile test, and the apparent loss in strength was simply a consequence of the extreme brittleness of the sample [13].

The yield strength of the FeCoCrNiMn HEA was significantly improved by a combination of carbon doping and subsequent decomposition. A yield strength of 1920 MPa and a 1.5% uniform elongation were obtained in this SCRed carbon-doped HEA as a result of the formation of nanosized $M_{23}C_6$ and $L1_0$ grains after being annealed at 500 °C for 1 h. Moreover, multi-stage heat-treatment processes could be designed using the decomposition kinetics for this HEA as a guideline.

4 Conclusions

(1) The decomposition sequence in the FeCoCrNiMn−1.3at.%C HEA was $M_{23}C_6$+$L1_0$, *B*2, and σ. Cr-rich $M_{23}C_6$ and σ phases formed in this carbon-doped HEA, contrary to the Cr-rich BCC phase that formed in carbon-free FeCoCrNiMn HEA.

(2) The decomposition kinetics of the *B*2, $L1_0$, and σ phases followed the Johnson−Mehl−Avrami−Kolmogorov equation. The FCC solid solution of the SCRed HEA was almost exhausted after being annealed for 32−64 d.

(3) The yield strength of the SCRed HEA increased from 1520 to 1920 MPa via the formation of nanosized $M_{23}C_6$ and $L1_0$ phases after being annealed for 1 h. However, failure occurred in the elastic regime during the tensile test because of the exhaustion of the FCC matrix after 64 d of annealing.

References

[1] GEORGE E P, RAABE D, RITCHIE R O. High-entropy alloys [J]. Nature Reviews Materials, 2019, 4(8): 515−534.

[2] GLUDOVATZ B, HOHENWARTER A, CATOOR D, CHANG E H, GEORGE E P, RITCHIE R O. A fracture-resistant high-entropy alloy for cryogenic applications [J]. Science, 2014, 345(6201): 1153−1158.

[3] LUO H, LI Z, RAABE D. Hydrogen enhances strength and ductility of an equiatomic high-entropy alloy [J]. Scientific Reports, 2017, 7(1): 1−7.

[4] CHENG Hu, XIE Yan-chong, TANG Qun-hua, RAO Cong, DAI Pin-qiang. Microstructure and mechanical properties of FeCoCrNiMn high-entropy alloy produced by mechanical alloying and vacuum hot pressing sintering [J]. Transactions of Nonferrous Metals Society of China, 2018, 28(7): 1360−1367.

[5] FU Jian-xin, CAO Cheng-ming, TONG Wei, PENG Liang-ming. Effect of thermomechanical processing on microstructure and mechanical properties of CoCrFeNiMn high entropy alloy [J]. Transactions of Nonferrous Metals Society of China, 2018, 28(5): 931−938.

[6] HE J Y, LIU W H, WANG H, WU Y, LIU X J, NIEH T G, LU Z P. Effects of Al addition on structural evolution and tensile properties of the FeCoNiCrMn high-entropy alloy system [J]. Acta Materialia, 2014, 62: 105−113.

[7] STEPANOV N D, SHAYSULTANOV D G, CHERNICHENKO R S, YURCHENKO N Y, ZHEREBTSOV S V, TIKHONOVSKY M A, SALISHCHEV G A. Effect of thermomechanical processing on microstructure and mechanical properties of the carbon-containing CoCrFeNiMn high entropy alloy [J]. Journal of Alloys and Compounds, 2017, 693: 394−405.

[8] KO J Y, HONG S I. Microstructural evolution and mechanical performance of carbon-containing CoCrFe-MnNi−C high entropy alloys [J]. Journal of Alloys and Compounds, 2018, 743: 115−125.

[9] PENG Jian, LI Zi-yong, FU Li-ming, JI Xin-bo, PANG Zhuo-rui, SHAN Ai-dang. Carbide precipitation strengthening in fine-grained carbon-doped FeCoCrNiMn high entropy alloy [J]. Journal of Alloys and Compounds, 2019, 803: 491−498.

[10] LI Zhi-ming. Interstitial equiatomic CoCrFeMnNi high-entropy alloys: Carbon content, microstructure, and compositional homogeneity effects on deformation behavior [J]. Acta Materialia, 2019, 164: 400−412.

[11] CHENG Hu, CHEN Wei, LIU Xiao-qiang, TANG Qun-hua, XIE Yan-chong, DAI Pin-qiang. Effect of Ti and C additions on the microstructure and mechanical properties of the FeCoCrNiMn high-entropy alloy [J]. Materials Science and Engineering A, 2018, 719: 192−198.

[12] KLIMOVA M, STEPANOV N, SHAYSULTANOV D, CHERNICHENKO R, YURCHENKO N, SANIN V, ZHEREBTSOV S. Microstructure and mechanical properties evolution of the Al, C-containing CoCrFeNiMn-type high-entropy alloy during cold rolling [J]. Materials, 2018, 53: 1−14.

[13] SCHUH B, MENDEZ-MARTIN F, VÖLKER B, GEORGE E P, CLEMENS H, PIPPAN R, HOHENWARTER A. Mechanical properties, microstructure and thermal stability of a nanocrystalline CoCrFeMnNi high-entropy alloy after severe plastic deformation [J]. Acta Materialia, 2015, 96: 258−268.

[14] OTTO F, DLOUHÝ A, PRADEEP K G, KUBĚNOVÁ M, RAABE D, EGGELER G, GEORGE E P. Decomposition of the single-phase high-entropy alloy CrMnFeCoNi after prolonged anneals at intermediate temperatures [J]. Acta Materialia, 2016, 112: 40−52.

[15] MA D, YAO M, PRADEEP K G, TASAN C, SPRINGER H, RAABE D. Phase stability of non-equiatomic CoCrFeMnNi high entropy alloys [J]. Acta Materialia, 2015, 98: 288−296.

[16] LI L, LI Z, KWIATKOWSKI DA SILVA A, PENG Z, ZHAO H, GAULT B, RAABE D. Segregation-driven grain boundary spinodal decomposition as a pathway for phase nucleation in a high-entropy alloy [J]. Acta Materialia, 2019, 178: 1−9.

[17] PICKERING E J, MUÑOZ-MORENO R, STONE H J,

JONES N G. Precipitation in the equiatomic high-entropy alloy CrMnFeCoNi [J]. Scripta Materialia, 2016, 113: 106−109.
[18] CHOUDHURI D, GWALANI B, GORSSE S, KOMARASAMY M, MANTRI S A, SRINIVASAN S G, MISHRA R S, BANERJEE R. Enhancing strength and strain hardenability via deformation twinning in FCC-based high entropy alloys reinforced with intermetallic compounds [J]. Acta Materialia, 2019, 165: 420−430.
[19] CHO K, FUJIOKA Y, NAGASE T, YASUDA H Y. Grain refinement of non-equiatomic Cr-rich CoCrFeMnNi high-entropy alloys through combination of cold rolling and precipitation of σ phase [J]. Materials Science and Engineering A, 2018, 735: 191−200.
[20] CHRISTOFIDOU K A, MCAULIFFE T P, MIGNANELLI P M, STONE H J, JONES N G. On the prediction and the formation of the sigma phase in CrMnCoFeNix high entropy alloys [J]. Journal of Alloys and Compounds, 2019, 770: 285−293.
[21] STEPANOV N D, YURCHENKO N Y, TIKHONOVSKY M A, SALISHCHEV G A. Effect of carbon content and annealing on structure and hardness of the CoCrFeNiMn-based high entropy alloys [J]. Journal of Alloys and Compounds, 2016, 687: 59−71.
[22] GU Ji, SONG Min. Annealing-induced abnormal hardening in a cold rolled CrMnFeCoNi high entropy alloy [J]. Scripta Materialia, 2019, 162: 345−349.
[23] PARK S, PARK C, NA Y, KIM H S, KANG N. Effects of (W, Cr) carbide on grain refinement and mechanical properties for CoCrFeMnNi high entropy alloys [J]. Journal of Alloys and Compounds, 2019, 770: 222−228.
[24] GUO Lin, OU Xiao-qin, NI Song, LIU Yong, SONG Min. Effects of carbon on the microstructures and mechanical properties of FeCoCrNiMn high entropy alloys [J]. Materials Science and Engineering A, 2019, 746: 356−362.
[25] CHEN L B, WEI R, TANG K, ZHANG J, JIANG F, HE L, SUN J. Heavy carbon alloyed FCC-structured high entropy alloy with excellent combination of strength and ductility [J]. Materials Science and Engineering A, 2018, 716: 150−156.
[26] FAN J T, ZHANG L J, YU P F, ZHANG M D, LIU D J, ZHOU Z, CUI P, MA M Z, JING Q, LI G, LIU R P. Improved the microstructure and mechanical properties of AlFeCoNi high-entropy alloy by carbon addition [J]. Materials Science and Engineering A, 2018, 728: 30−39.
[27] SHAHMIR H, HE J, LU Z, KAWASAKI M, LANGDON T G. Effect of annealing on mechanical properties of a nanocrystalline CoCrFeNiMn high-entropy alloy processed by high-pressure torsion [J]. Materials Science and Engineering A, 2016, 676: 294−303.
[28] WILLIAMSON G, HALL W. X-ray line broadening from filed aluminium and wolfram [J]. Acta Metallurgica, 1953, 1: 22−31.
[29] WILLIAMSON G, SMALLMAN R. III. Dislocation densities in some annealed and cold-worked metals from measurements on the X-ray debye-scherrer spectrum [J]. Philosophical Magazine, 1956, 1: 34−46.
[30] MATSUI I, UESUGI T, TAKIGAWA Y, HIGASHI K. Effect of interstitial carbon on the mechanical properties of electrodeposited bulk nanocrystalline Ni [J]. Acta Materialia, 2013, 61: 3360−3369.
[31] HE J Y, WANG H, HUANG H L, XU X D, CHEN M W, WU Y, LIU X J, NIEH T G, AN K, LU Z P. A precipitation-hardened high-entropy alloy with outstanding tensile properties [J]. Acta Materialia, 2016, 102: 187−196.
[32] LAPLANCHE G, BERGLUND S, REINHART C, KOSTKA A, FOX F, GEORGE E P. Phase stability and kinetics of σ-phase precipitation in CrMnFeCoNi high-entropy alloys [J]. Acta Materialia, 2018, 161: 338−351.
[33] CHRISTIAN I. The theory of transformations in metals and alloys [M]. Oxford: Pergamon Press, 1965.

含碳 FeCoCrNiMn 高熵合金的中温分解动力学

彭 健[1]，李紫勇[1]，冀新波[1]，孙衍乐[1]，付立铭[1,2,3]，单爱党[1,2,3]

1. 上海交通大学 材料科学与工程学院，上海 200240；
2. 上海交通大学 先进船舶和深海勘探协同创新中心，上海 200240；
3. 上海交通大学 上海高温材料与精密成形重点实验室，上海 200240

摘 要：研究大变形冷轧 1.3 at.%碳掺杂等摩尔比 FeCoCrNiMn 高熵合金在 500 °C 退火下的相分解动力学和相应的力学性能演变。该高熵合金为面心立方结构(FCC)的单相固溶体，随着退火时间的延长，合金中先析出 $M_{23}C_6$+$L1_0$，随后析出 *B*2，最后析出 σ 相。$L1_0$、*B*2 和 σ 相的分解动力学遵循 Johnson−Mehl−Avrami−Kolmogorov (JMAK)方程。冷轧后 FCC 结构高熵合金的屈服强度为 1520 MPa；在 500 °C 下退火 1 h 后，合金中析出纳米尺寸的 $M_{23}C_6$ 和 $L1_0$ 相，合金的屈服强度可达 1920 MPa；当退火时间延长至 2 d 时，合金中析出的 $M_{23}C_6$ 和 $L1_0$ 相体积分数增大且晶粒粗化，合金的强度和塑性均下降；退火 4~32 d 后，*B*2 和 σ 相的析出使合金的硬度增加；退火 32~64 d 后，合金几乎全部由 FCC 相分解成 $M_{23}C_6$、$L1_0$、*B*2 和 σ 相，此时合金的硬度约为 HV 760。该合金的分解动力学可用于指导含碳高熵合金的热处理。

关键词：FeCoCrNiMn；高熵合金；分解动力学；力学性能；碳掺杂

(Edited by Wei-ping CHEN)